CrossMark

An adjoint-based FEM optimization of coseismic displacements following the 2011 Tohoku earthquake: new insights for the limits of the upper plate rebound

Fabio Pulvirenti [a], Shuanggen Jin [b], Marco Aloisi [c,*]

[a] *Comsol Multiphysics GmbH, 37073 Gottingen, Germany*
[b] *Shanghai Astronomical Observatory, Chinese Academy of Sciences, Shanghai 200030, China*
[c] *Istituto Nazionale di Geofisica e Vulcanologia, Osservatorio Etneo, Catania, Italy*

A R T I C L E   I N F O

A B S T R A C T

The 11 March 2011 Tohoku earthquake was the strongest event recorded in recent historic seismicity in Japan. Several researchers reported the deformation and possible mechanism as triggered by a mega thrust fault located offshore at the interface between the Pacific and the Okhotsk Plate. The studies to estimate the deformation in detail and the dynamics involved are still in progress. In this paper, coseismic GPS displacements associated with Tohoku earthquake are used to infer the amount of slip on the fault plane. Starting from the fault displacements configuration proposed by Caltech-JPL ARIA group and Geoazur CNRS, an optimization of these displacements is performed by developing a 3D finite element method (FEM) model, including the data of GPS-acoustic stations located offshore. The optimization is performed for different scenarios which include the presence of topography and bathymetry (DEM) as well as medium heterogeneities. By mean of the optimized displacement distribution for the most complete case (heterogeneous with DEM), a broad slip distribution, not narrowly centered east of hypocenter, is inferred. The resulting displacement map suggests that the beginning of the area of subsidence is not at east of MYGW GPS-acoustic station, as some researchers have suggested, and that the area of polar reversal of the vertical displacement is rather located at west of MYGW. The new fault slip distribution fits well for all the stations at ground and offshore and provides new information on the earthquake generation process and on the kinematics of Northern Japan area.

© 2014 Elsevier B.V. All rights reserved.

1. Introduction

The growth of Japanese arc has been the result of the subduction process of the ancient Pacific Ocean floor since the Permian age. The actual shape is the outcome by the backarc basin formation in the Tertiary (Taira, 2001). Understanding the dynamic of the subduction processes is particularly important since it is principally along the plate boundaries that the seismic activity is concentrated. Monitoring these processes is also a valuable endeavor in tackling natural hazards and preventing risks for the population. The dense ground observations provide important data to monitor the crustal deformation and understand its process, including a dense GPS network of over 1000 stations and a dense seismic network with more than 1800 stations, together with many other crustal deformation measurement systems including InSAR, strong motion, teleseismic and tsunami detection systems.

At 05:46 UTC, 11 March 2011, a strong M_w 9.0 earthquake struck off the northeastern coast of Honshu, Japan. It was the strongest event in the seismic history of Japan and, for this reason, completely unexpected. Indeed, in terms of stress release, the catalogue of historical seismicity of Japan does not include a similar event. Moreover, no clear signal of preseismic tilt change or preslip was found (Hirose, 2011). A prediction of a $M \geqslant 8.0$ earthquake, with an intermediate-term (several years; usually five) narrow-range (areas of linear dimension 2–3 times the earthquake source zone size) accuracy, in the area of the M 9.0 Tohoku-Oki event, was made using a combined algorithm called M8-MSc (Davis et al., 2012). These pattern recognition methods are based on premonitory seismicity patterns and were designed by the retroactive analysis of seismicity preceding the greatest ($M \geqslant 8.0$) earthquakes worldwide (M8 method) or of the regional seismic catalogue prior to the Eureka earthquake (1980, $M = 7.2$) near Cape Mendocino in California (MSc method). The M8 method evaluates, every six months, the number of earthquakes (seismic flux rate), its

* Corresponding author.

deviation from long-term trend (differential of rate, i.e. acceleration), the linear concentration of sources and earthquake clustering. The algorithm MSc provides a second approximation to M8, and it is applied whenever the seismicity is sufficiently high to allow the algorithm to be used, strongly reducing the alarm area to a narrow or exact range. In particular, the MSc method evaluates the areas where seismicity is high but irregular, interrupted by short intervals of anomalous quiescence. See Davis et al. (2012) and the web site http://www.mitp.ru/en/, for more details. The prediction of a $M \geqslant 8.0$ earthquake was initially announced in mid-2001 and, successively, in January 2011, only 70 days before the Tohoku-Oki event, the algorithm detected a small change in the concentration of sources. It accurately identified the March 11, 2011, magnitude 9.0 Tohoku Earthquake, however it was not used, in part due to the predictions limited distribution and in part to the lack of applying existing methods for intermediate-term predictions which can be used to make decisions for taking actions.

Studies conducted using teleseismic ocean reverberations and applied to the first 4 s of the event (Chu et al., 2011) suggest that the Tohoku-Oki earthquake started as a small M_w 4.9 event and then evolved into a slower extremely large slip event up-dip. The Japan Meteorological Agency (hereafter JMA) reported the following hypocenter location: Lat 38.05°N, Long 142.8°E and depth 24 km (b.s.l.). The results of the CMT analysis indicates a reverse fault type mechanism with WNW–ESE compressional axis, in accordance with the direction of the Pacific Plate, which subducts under the Okhotsk Plate at a rate of about 8–9 cm/year (DeMets et al., 1990; Wei and Seno, 1998). The event was preceded by a M_w 7.3 foreshock (38.440°N, 142.840°E on 9 March 2011 at 02:45:20.28 UTC; USGS) and followed by more than 680 aftershocks estimated by the JMA.

The dynamic of this event has been widely investigated by many researchers, using different techniques (e.g., http://supersites.earthobservations.org/sendai.php). Most of these studies have focused on finite fault models by inversion procedures (Ide et al., 2011; Yoshida et al., 2011; Ozawa et al., 2011) or by Bayesian inference using a large number of forward models (Simons et al., 2011) in order to infer the location and size of the source. Despite the use of a large dataset, including GPS (on land and offshore) (Fujita et al., 2006; Sato et al., 2011; Kyriakopoulos et al., 2013), geological (Minoura et al., 2001), teleseismic (Chu et al., 2011; Zhang et al., 2011; Lay et al., 2011a), tsunami (Fujii et al., 2011), strong motion (Zahradnik et al., 2011), InSAR (Liu and Yamazaki, 2011) or combined techniques (e.g., Ammon et al., 2011; Koketsu et al., 2011; Yoshida et al., 2011; Yokota et al., 2011; Kobayashi et al., 2011; Gusman et al., 2012; Lee, 2012; Romano et al., 2012; Amici et al., 2013; Wang et al., 2013) the results are fairly different. Almost all studies, in fact, agree in describing the Tohoku-Oki earthquake as an M_w 9.0 event generated on a fault plane located at the interface between the Okhotsk Plate and the subducting Pacific Plate, but the inferred size, position (e.g., strike, dip and rake) as well as the way it ruptured and the maximum slip are not the same. Generally, the fault plane is inferred to have a strike angle between 192° and 202° and a fixed dip angle between 9° and 14°, although some authors consider also variable angles from 5° up to 20° (e.g., Yokota et al., 2011; Gusman et al., 2012).

The inferred size of the fault plane ranges between 300 km × 150 km (mainshock area) to 500 km × 250 km (including aftershocks area), while the maximum slip varies between 20 and 60 m. These differences are because inversion procedures strongly depend on the type and quality of the data used and on the rheological properties of the medium where the inversion is performed (e.g., homogeneous half-space versus a heterogeneous elastic medium).

In this paper, we use, as starting model, the solutions achieved by Caltech-JPL ARIA group and Geoazur CNRS (hereafter called

"initial solution" provided by CJAGC), which give information on the area and displacement configuration of the fault plane. In particular, the inferred fault slip distribution allows to fit well the inland GPS recorded data. For this reason, we use the solution as a starting point for a new inversion, which includes both GPS and offshore data, performed through a numerical model based on the finite element method (hereafter, FEM). Results of inversion procedures can be in fact improved by using FEM because, under proper boundary conditions (which depend on the area of study), finite element models have the possibility of well approximating the geometry of the plates and of considering how the solution changes along each part of them as well as evaluating how the changes in the rheological properties or the presence of the topography affect the solution at the surface. Indeed, the finite element approach allows us to consider a more realistic approximation of the slip estimation by introducing both lateral and vertical variations of the elastic properties and the presence of topography (for other similar studies about large subduction earthquakes see, e.g., Trubienko et al., 2013).

As well known in literature (e.g., Cattin et al., 1999; Masterlark 2003; Aloisi et al., 2011; Hsu et al., 2011), the simple analytical model approach (homogeneous, isotropic, Poisson-solid half-space assumption) has in fact strong limitations and introduces significant displacement prediction errors (with respect to measurement uncertainties). In particular, Cattin et al. (1999) found that rigidity contrasts, existing within the upper crust can increase the horizontal displacements for a given slip model by up to 40%. Therefore, avoiding to take into account the effect of an existing low-rigidity layer leads to an underestimation of the seismic moment release and produces errors in the estimation of fault depth and slip from coseismic geodetic data. Masterlark (2003) asserts that the widely accepted homogeneous, isotropic, Poisson-solid half-space assumptions poorly approximate subduction zone systems of converging oceanic and continental crust. Hsu et al. (2011) affirms that topographic effects can be significant near a trench and slip distribution is strongly influenced by 3D variations of material properties, although the fit to surface observations in the 3D FEM model could be similar to that from a simple half-space model. Because of the related complexity, some of these aspects have been rarely implemented in previous studies.

2. Tectonic setting

The Japanese arc system is rather complex and related to the interaction of several plates. Five plates are generally identified: the Eurasia, Amur, Okhotsk, Pacific, and Philippine Sea plates but the exact shape and margin of these plates are still controversial (Heki et al., 1999; Jin et al., 2007; Zhao et al., 2011). The 11 March 2011 Tohoku Oki interplate earthquake, a M_w 9.0 event, struck at 05:46:23 UTC off the northeastern Japan coast, where the Pacific plate moves northwestward at a rate of about 8–9 cm/year, subducting beneath northern Honshu island from the Japan trench (Fig. 1).

3. Methods and data

In this section, the methods to develop our FEM model are described. As aforementioned, the finite fault inversion solution provided by CJAGC, called "initial solution", (http://www.tectonics.caltech.edu/slip_history/2011_taiheiyo-oki/#slip) is used as initial slip estimation to be optimized in our model. The "initial solution" is the result of the inversion of Global Seismographic Network broadband data and GPS data (Ji et al., 2002). The hypocentral location estimation was based on the JMA estimate (Lat 38.05°N, Long 142.8°E, depth 24 km, b.s.l.). The dip angle for the slab was taken from the National Earthquake Information Center (NEIC)
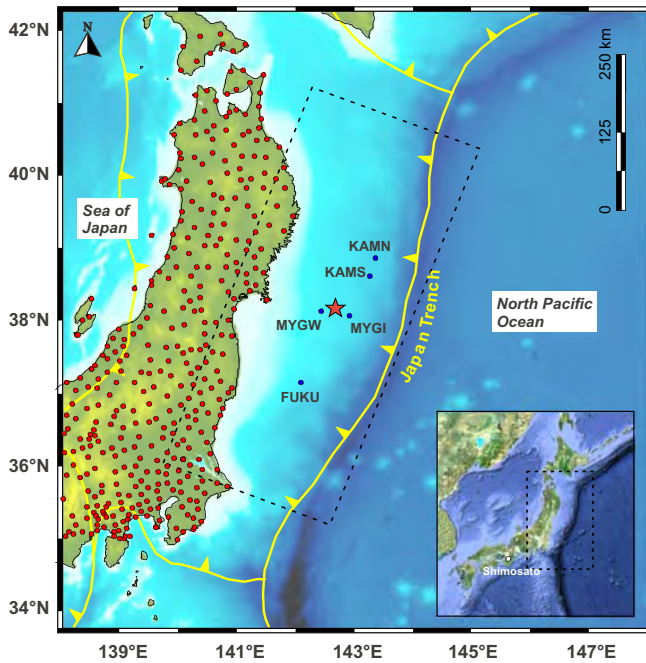
Fig. 1. General view of NE Japan (Honshu island) including the GPS stations (red points), the offshore acoustic transponders (blue points), the Japan trench and the fault plane used in our work (dashed rectangle). An overview of Japan with Shimosato reference point is shown in the inset. Red star indicates the earthquake epicenter. (For interpretation of the references to colour in this figure legend, the reader is referred to the web version of this article.)

Fig. 2. Digital Elevation Model (a) and geometry of the subduction zone with the mesh (b) used for the models. The number of degrees of freedom is 215,115. DEM emphasized five time, for more clarity.

W-phase solution (dip 9°) and the 1D velocity model was extracted from the CRUST2.0 global tomography model (Bassin et al., 2000). To match the orientation of the subduction zone in the area of maximum slip, a fault strike of 201° was used. The size of the inferred rupture plane is compatible with the area of aftershock distribution.

Our FEM approach is divided in two parts. The first is a simple validation of the FEM reference system. The first test is made in order to verify if the agreement between the "initial solution" and the surface displacements of GPS stations with respect to the recorded displacements is still kept in the chosen FEM geometry. The second part is the optimization of the original slip values on the mega thrust interface including the information of seafloor data by five acoustic transponders located near the epicenter. The aim of this work is to see how the starting solution ("initial solution") changes when offshore displacements data are included and when the contribution of topography and heterogeneities is considered and to see how this new slip configuration can be interpreted to better understand the dynamic of the subduction process and the implications on the kinematics of the northern Japan area.

3.1. FEM setup

The FEM model has been developed with the finite element software COMSOL Multiphysics version 4.3a (http://www.comsol.com). The computational domain has a size of $800 \times 900 \times 200$ km^3, where we included the topography and the medium heterogeneities. With this choice, our model covers the area between 137°E and 145.3°E of longitude and 34.4° and 42.3°N of latitude. It includes the northern part of Honshu island and the southern part of Hokkaido island (Hakodate), together with the offshore area, along the Japan trench (Figs. 1 and 2). This ensures that the part of the Pacific slab, to which the fault plane belongs, is included, as well as the part of the Japan coast where
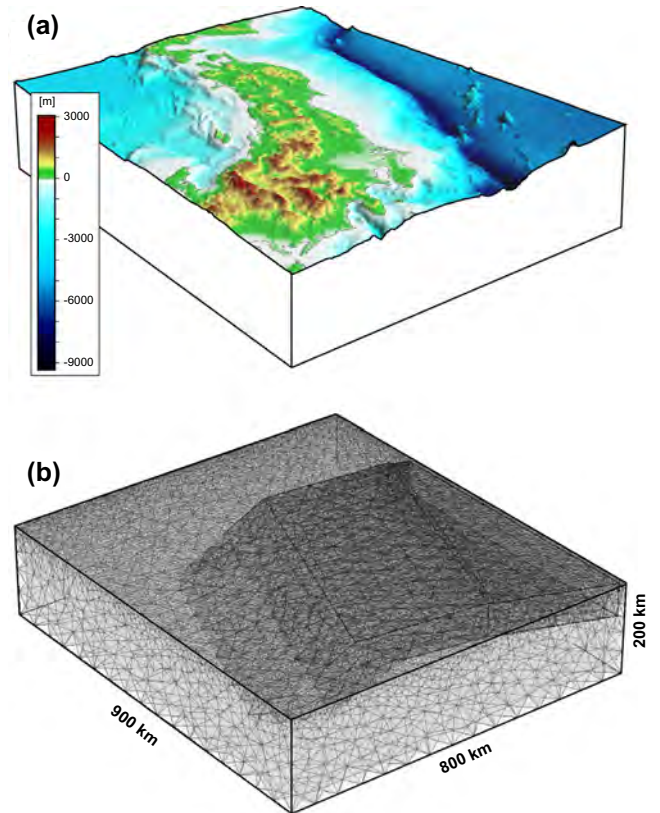
the chosen GPS stations used for the optimization procedure are located (Fig. 1). With the aim of verifying if the deformation field is reproduced with an acceptable accuracy in our numerical domain, we performed a comparison between the analytical and numerical displacements evaluating the analytical solution achieved by a uniform coseismic slip in a homogeneous material half-space (Okada, 1985), and the numerical one achieved by the same coseismic slip in a homogeneous FEM domain, with a flat free surface. In order to properly compare the FEM domain with the Okada half-space model assumption, we applied an "Infinite Element Domain" condition. This approach applies a rational coordinate scaling to a layer of virtual domains, surrounding the computational domain. The finite elements are stretched in the normal direction such that the boundary conditions on the outside of the infinite element layer are effectively applied at a very large distance from any region of interest. The obtained maximum differences between the two solutions, calculated on the free surface, are of the order of few centimetres.

Inside the domain, a part of the Pacific slab is inserted (Fig. 2). The shape, limits and orientation of the slab are based on the results of tomography data of Hasegawa et al. (2005; see profile e) and Nakajima and Hasegawa (2006) and on the FEM profile modelled by Suito et al. (2002). The depth of the slab varies from 10 km b.s.l., out of the trench, up to 200 km b.s.l., on the most western part. The fault plane considered in our model has the same position, size, strike and dip angle as suggested by the "initial solution" (http://www.tectonics.caltech.edu/slip_history/2011_tai-heiyo-oki/update/static.txt).

The "initial solution" provided by CJAGC is, in particular, the composition of the displacements of 350 patches (25×14), each having the same size of 25×20 km, strike (201°) and dip angle

(9°), but with different rake. In the FEM model, these displacements are applied to the hanging wall boundary only in the form of a stationary (instantaneous) prescribed displacement which represents the abrupt rebound of the continental crust in the post-locked phase, when the rupture has been generated. In particular, basing on the rake, the displacement is applied in the two directions tangent to the fault plane (about N110°E for the dip-slip component and about N20°E for the strike-slip component). Mathematically, this is done through two interpolation functions, each of which assigns a value of displacement for the above mentioned dip-slip and the strike slip components to the (x,y) coordinate of several points in the hanging wall boundary, each of which located in the same position to the patch centers of the "initial solution". The values of the dip-slip and strike-slip displacements among the other parts of the hanging wall boundary are interpolated through the nodes.

Because the displacement of the hanging wall during the rebound is much faster than the footwall and because we are solving it with a stationary study, the footwall tangential displacement can be avoided. However, in order to assure that no interpenetration of the two parts occurs, a roller condition is applied to the hanging wall and to the footwall in the form "$\mathbf{u} \cdot n = \mathbf{0}$", where $\mathbf{u}$ denotes the displacement and the vector n is the outward unit normal to the fault plane. The completion of the necessary boundary conditions (e.g., Pergler and Matyska, 2007) to properly constrain the model is finally given by the application of a continuity condition, this is an internal feature of Comsol, which assures the continuity of the dependent variables (in terms of the degrees of freedom at the nodes) over the interface.

The other boundary conditions are set as follows: the domain top boundary is set as free, the bottom surface at 200 km b.s.l. is fixed and a roller condition is imposed to the lateral external boundaries.

The mesh is made up of tetrahedral linear elements and is refined at the surface and onto the fault plane, in order to improve the accuracy of the solution. A control of the mesh quality was made in order to assure a good refinement. The total number of degrees of freedom is 215, 115 (Fig. 2).

The simulation includes a Digital Elevation Model (DEM) from (Smith and Sandwell, 1997). The DEM takes into account the Japan land and the bathymetry (Fig. 2). Data are collected for the area of interest, re-sampled and interpolated with a 3 km resolution and, successively, imported into the model in the form of a parametric surface.

The physical parameters are set in order to consider two possible types of physical conditions for the domain: (1) a layered velocity model for the crust down to Moho discontinuity together with an isotropic "Preliminary Reference Earth Model", hereafter PREM, (Dziewonski and Anderson,1981) under Moho discontinuity and (2) a full heterogeneous domain including Moho and Conrad discontinuities (Zhao et al., 1992; 1994; 1997; Zhao, 2009).

3.2. FEM reference frame test: the direct model

In order to evaluate the validity of the "initial solution" in our FEM domain, a direct model is run. In this phase, the "initial solution" is used as a prescribed displacement onto the fault plane in the form of two functions (dip-slip and strike-slip components; opening is prescribed to zero) which interpolate linearly at the mesh nodes the given slip values of the 350 points provided by CJAGC. To consider the same conditions used in the finite fault inversion procedure performed by CJAGC, the DEM is not taken into account and only laterally homogeneous, elastic parameters are set in the form of a layered velocity model for the crust above Moho discontinuity (Table 1) plus the data of the PREM (Dziewonski and Anderson, 1981) under Moho discontinuity.

Table 1
Seismic velocities and density values for the layered velocity model of the crust.

v_p (km/s)	v_s (km/s)	Density (g/cm³)	Thickness (km)
4.40	2.510	2.0	4.0
6.00	3.460	2.6	10
6.70	3.870	2.9	16
7.70	4.500	3.3	22.5

The prescribed slip distribution was applied to the fault plane belonging to the upper crust, generating the displacement of the surface above the slab. In particular, we look at the coseismic displacements at 377 GPS stations (see Ozawa et al., 2011 – supplementary information, table S1) and compare the numerical results to the recorded ones (Figs. 3a and b). The general accordance between the FEM and recorded GPS vectors, both for the horizontal and vertical displacements, means that the "initial solution" is a good starting point even in the FEM setting.

Sea bottom displacements data in five locations around the epicenter have been published (for details see Sato et al., 2011; reference point located at Shimosato, see inset in Fig. 1). Even if only five stations are considered, the contribution of these stations to the overall displacement pattern is high because their location is very close to the epicenter, so the inclusion of these stations is very useful in providing new constraints to quantify the amount of slip on the rupture plane, where GPS stations cannot measure. For this reason, offshore measurements data have been included also in other recent works (e.g., Grilli et al., 2012; Gusman et al., 2012; Iinuma et al., 2012).

We first checked if the "initial solution" is capable of predicting the offshore displacements. The comparison between the displacements at the five acoustic transponders offshore obtained from the "initial solution" and the recorded data shows a big disagreement (see Table 2 and, for more details, Paragraph 3.4).

Consequently, the slip distribution provided by the "initial solution" is not suitable to explain the offshore displacements. Therefore, this fault slip distribution needs to be improved in order to match the displacements offshore too.

In our work, an optimization procedure is performed with a highly realistic FEM model which, as said before, can take into account both for the topographic relief and for the medium heterogeneities, as constrained by tomographic data. The optimization method is based on the SNOPT code (Gill et al., 2006), directly implemented in COMSOL Multiphysics software. It can be used to solve shape, size, and topology optimization problems, as well as inverse problems such as parameter estimation. In particular, the Optimization Module computes the analytic sensitivities of an objective function to the design variables, considers any constraints imposed upon the problem and uses a gradient-based optimization technique to find the optimal FEM solution. To compute the gradient efficiently an adjoint method is then used.

3.3. FEM optimization setting

The GPS coseismic displacement, for 377 ground stations plus 5 offshore acoustic transponders, are imposed in the form of an objective function applied only to the top boundary of the FE domain (the free surface), so the objective equation (A.5), reported in the supplementary materials, reduces to the term Q2 which has the following form:

$$Q_2 = \int_\Omega q_2 d\Omega. \tag{1}$$

where

$$q_2 = \frac{(u - u\_obs(x,y))^2 + (v - v\_obs(x,y))^2 + (w - w\_obs(x,y))^2}{\sigma_0} \tag{2}$$
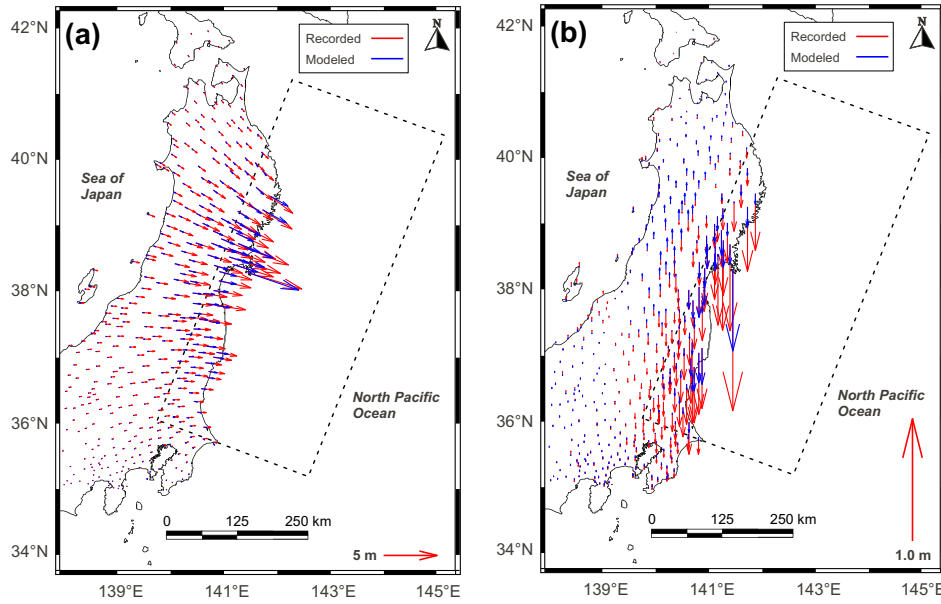
Fig. 3. (a) Comparison between the observed and the modelled horizontal displacement vectors at GPS stations for the direct FEM model. (b) Comparison between the observed and the modelled vertical displacement vectors at GPS stations for the direct FEM model.

Table 2
Comparison between observed and modelled (direct FEM model) coseismic displacements at offshore stations (values are in meters).

Station	dx Observed	dy Observed	dz Observed	dx FEM direct	dy FEM direct	dz FEM direct
MYGI	22.32	−9.93	3.14	19.24	−3.53	1.12
KAMN	14	−5	1.61	17.52	4.83	3.18
KAMS	21	−9	1.49	22.63	2.70	2.79
MYGW	14	−5	−0.78	13.72	−3.83	2.25
FUKU	4	−2	0.86	5.81	−4.26	−0.56

In particular, $u\_obs(x, y)$, $v\_obs(x, y)$ and $w\_obs(x, y)$ are functions which interpolate linearly the values of each component x, y, and z of the recorded displacements at the free surface computed numerically (u, v, w), as consequence of the previously prescribed displacements, applied to the fault plane. The value σ_0 (0.1 m) is the mean standard deviations between the ground stations and the offshore stations. As previously mentioned, the starting slip configuration used on the fault plane is the one that corresponds to the "initial solution" which considers the fault plane as formed by 350 sub-faults with different rake (see Paragraphs 3.1 and 3.2). The total displacement of each sub-fault is then decomposed in the two directions tangent to the fault plane in the form of two functions dip-slip(x, y) and strike-slip(x, y) which interpolate the 350 values with respect to the respective directions (about N110°E for dip-slip and N20°E for strike-slip). As said before, no normal components are considered, because the focal mechanism shows a governing dip inverse slip. To optimize the initial slip configuration, the functions dip-slip(x, y) and strike-slip(x, y) are multiplied by two dimensionless control variables called v_1 and v_2, respectively. The role of these two variables is to drive the displacements onto the mesh nodes in order to minimize the Eq. (2). In particular, for each mesh node, SNOPT finds, the optimal value for v_1 and v_2, while an interpolation is made between the nodes. The values of dip-slip(x, y) and strike-slip(x, y), extrapolated by the "initial solution" and multiplied by v_1 and v_2, represent the new optimized coseismic displacement. The starting value of v_1 and v_2 is 1 and then is automatically adjusted, where the slip configuration needs to be changed, among these ranges:

$$0 \leq v_1 \leq 2$$
$$-2 \leq v_2 \leq 2 \qquad (3)$$

The choice of the lower and upper values for v_1 and v_2 are generally arbitrary but a better choice is necessary to avoid wasting computational time, optimizing on big ranges. Because the fault mechanism is principally inverse and the hanging wall moves mainly towards about N110°E direction, only positive values have been assigned to the dip-slip component up to +2 (double displacement) while positive and negative values are given for the strike-slip component, because the rupture broke in two opposite directions. Considering a range which covers up to a double value of displacement with respect to the starting displacement configuration of the "initial solution", we conjecture that the chosen constraints are reasonable. Finally, in order to avoid underdamping of the solution (big oscillations of the displacement field variable over short distances), we included two additional constraints, one for each of the gradients of v_1 and v_2. The additional constraints are defined over the fault plane in terms of the following constraint expressions:

$$dtang(v_1, x) + dtang(v_1, y) \qquad (4)$$

and

$$dtang(v_2, x) + dtang(v_2, y) \qquad (5)$$

Where (4) and (5) are the linear combinations, with respect to x and y direction, of the tangential differentiations of the two control variables "v_1" and "v_2", respectively. The chosen lower and upper bounds for these expressions are ±5.0E0−5 for the expression (4) and ±2.5E−05 for expression (5). These values have been chosen after examination of the trade-off curves comparing model variance and data standard deviation for different damping values (Fig. 4)

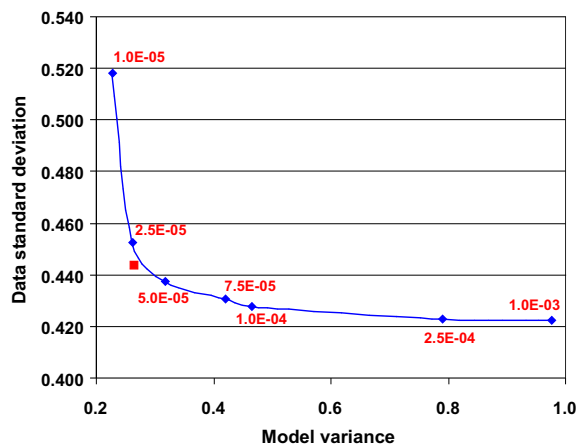and following the approach proposed by Eberhart-Phillips (1986); see also Aloisi et al. (2002).

After setting the optimization, a sensitivity test, in order to check that the PDE model and the optimization variables are set up correctly was also performed.

3.4. Performed models

Three simulations are performed, in order to evaluate how the fault slip distribution of the "initial solution" changes when co-seismic displacements are optimized for the GPS stations and the acoustic transponders together, with respect to different rheological properties and the presence of topography and bathymetry. As mentioned before, two different physical configurations are considered: (1) a stratified model (layered velocity model with isotropic PREM) and (2) a full heterogeneous domain where precise v_p and v_s seismic velocities data are used. Moreover, the presence of the DEM is also considered.

The first simulation is the optimization of the "initial solution" adding the data of the 5 acoustic transponders to the previously used 377 GPS inland stations. In this case, a stratified model with no DEM, like the one used by CJAGC has been considered. This configuration is used to see how the slip distribution given by the "initial solution" changes only for the presence of the acoustic transponders, which drive the displacements around the earthquake epicenter (compare "a" and "b" parts in Fig. 5).

In the second simulation, a full heterogeneous model is considered without DEM. In this case, we use the v_p and v_s seismic velocity data of Zhao (2009) by which a 3-D P-wave velocity distribution beneath the Japan Islands have been obtained by a simultaneous inversion of arrival time data from local, regional and teleseismic events and in which Moho and Conrad discontinuities profiles are also included (Zhao et al., 1992). In our manuscript, the elastic parameters are estimated from these data by using the density-wave velocities empirical laws of (Christensen and Mooney, 1995) and, in particular, the linear velocity-density regression line parameters set for all rocks up to 50 km depth (see their Table 7). The parameters at 50 km are ascribed to the underlying domain. Data files are sorted by depth in 9 levels (0, 10, 25, 40, 65, 90, 120, 160 and 200 km, b.s.l.) for each parameter (density, Young's modulus and Poisson's ratio) and then re-sampled in a 3 km grid

to acquire the variation of density, Young's modulus and Poisson's ratio inside the domain (a sample in Fig. 6). The values at intermediate levels are an interpolation of the principal ones.

The final simulation considers the heterogeneous case with the DEM. When the DEM is added, the objective function is referred to the parametric surface while the variables are defined on the undeformed fault plane, whose position and angle are fixed a priori. In this case, all the stations displacements are evaluated at their real heights, both at ground and offshore on the sea bottom.
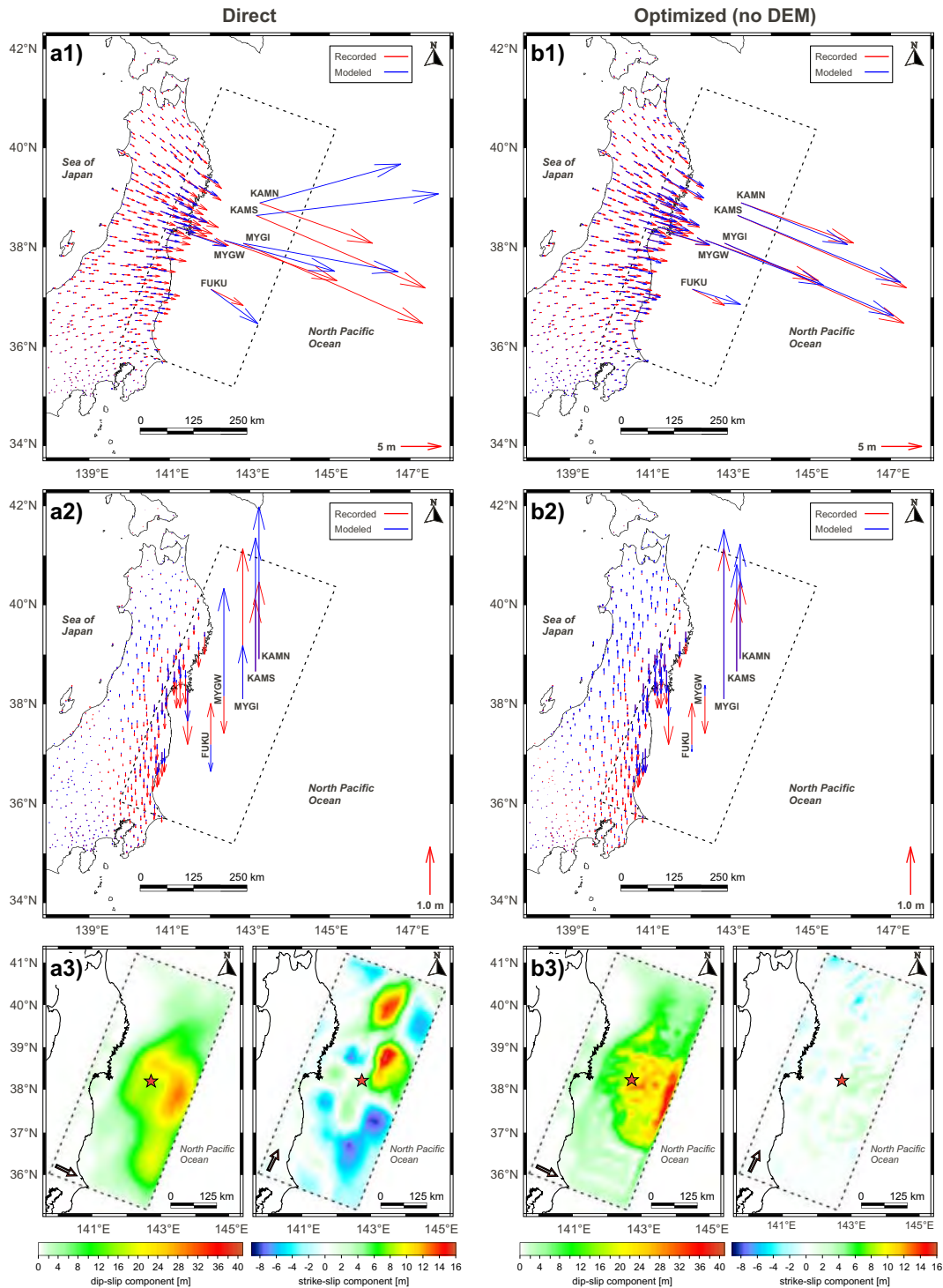
3.5. Reliability of inversion

Checkerboard tests were performed to quantify the resolution of our results and to study the contribution of the topography, the 3D heterogeneities and, finally, of onshore and offshore geodetic data (e.g., Aloisi et al., 2002; Yokota et al., 2011; Kyriakopoulos et al., 2013). We used two different checkerboard inputs: (1) 5 × 3 patches with slip 0 or 20 m; (2) 10 × 4 patches with slip 0 or 1 m. We generated synthetic datasets for the checkerboard slip distribution shown in Fig. 7a and d. Successively, these synthetic datasets, randomly perturbed according to the uncertainties of the experimental data, were inverted using the same parameters as those for our inversions. We obtained that SNOPT algorithm is able to find the same slip distribution almost independently of the complexities that we use. In particular, it obtains a slightly better result when we consider the 3D heterogeneities in our model (reconstruction of patches 0.2%, that is 336 km^2, more than the stratified layered velocity model). The better performance obtained by SNOPT in the heterogeneous case demonstrates the importance of using a more realistic model, especially in a case as Tohoku-Oki earthquake, occurred in an area where strong 3D heterogeneities are present (Fig. 6). Moreover, it demonstrates the power of SNOPT to work also in very complex problems.

Regarding the contribution of both geodetic data on the resolution of estimated slip values (Fig. 7), adding the offshore data, we obtain an increment of patches reconstruction of about 10% (equivalent to 16,800 km^2), in both the checkerboard tests. In particular, the addition of seafloor geodetic data increases the resolution in the central sector of our fault model, near the trench. This result demonstrates the importance of the use of offshore data in the evaluation of the slip distribution. We retain that the sector of good resolution covers the zone where we obtain some important results.

4. Results

One of the main results of our investigation is showed in Fig. 5. Parts "a1" and "b1" show the comparisons between the recorded and modelled horizontal components of the displacement vectors at the ground GPS stations and at the offshore stations ("acoustic transponders") for the direct model ("initial solution") and for the optimized model (stratified without DEM), respectively. The comparisons of these two models for the vertical component of the displacement vectors at the GPS and offshore stations are instead shown in Fig. 5, parts "a2" and "b2".

The direct model shows a good general accordance between the numerical (blue) and recorded (red) horizontal vectors at GPS stations, but not for the stations offshore, where the modelled vectors at KAMN, KAMS, MYGY and MYGW stations are about NE oriented instead of SE oriented, while the vector at FUKU station is oriented SSE instead of SE. Modelled vertical displacement vectors at KAMN and KAMS have a larger amplitude than observed ones, as well as MYGW, which is positive instead of negative and with a big amplitude. Modelled vertical displacement vector at MYGI has a very small amplitude with respect to the observed one and, at FUKU,

Fig. 4. Data standard deviation *vs.* model variance for different damping values (red numbers). The data standard deviation measures the goodness of the fit between the recorded and modelled data. Model variance, calculated as the mean variance between the variance of dip-slip and the variance of strike-slip on the fault plane, measures the complexity of the fault slip deduced by FEM optimization. Damping values of 5.0E0−5 and 2.5E−05 were here assumed for v_1 and v_2, respectively (red square). (For interpretation of the references to colour in this figure legend, the reader is referred to the web version of this article.)

Fig. 5. Comparison between the displacement vectors at GPS and offshore stations and the fault slip distribution as computed before the optimization (parts "a", Direct) and after the optimization (parts "b", Optimized Stratified - no DEM). (a1) Horizontal displacement vectors for the "initial solution"; (a2) Vertical displacement vectors for the "initial solution"; (a3) Original slip distribution onto the fault plane showing the dip-slip component (left) and the strike-slip component (right). (b1) Horizontal displacement vectors for the optimized solution (stratified model – no DEM); (b2) Vertical displacement vectors for the optimized solution (stratified model – no DEM); (b3) Optimized slip distribution onto the fault plane showing the dip-slip component (left) and the strike-slip component (right). Red arrows in the bottom figures indicate the positive direction for the tangential components. Red star indicates the earthquake epicenter. (For interpretation of the references to colour in this figure legend, the reader is referred to the web version of this article.)

it shows opposite direction. We refer the reader to Table 2 for a quantification of these displacements.

Our optimization procedure is able to redistribute the slip onto the fault plane (Fig. 5, "b3") getting a more adequate estimation respect to the original one (Fig. 5, "a3"). In particular, the displacement of the component dip-slip is now augmented in the most

eastern central part of the fault plane and decreased in the south-eastern part. This combination fixes the amplitude of the modelled horizontal vectors in the central part and reduces the amplitude of the vector at FUKU station. The component strike-slip is instead greatly reduced, near to zero meters, in order to let the offshore stations (except FUKU) turn clockwise to match the
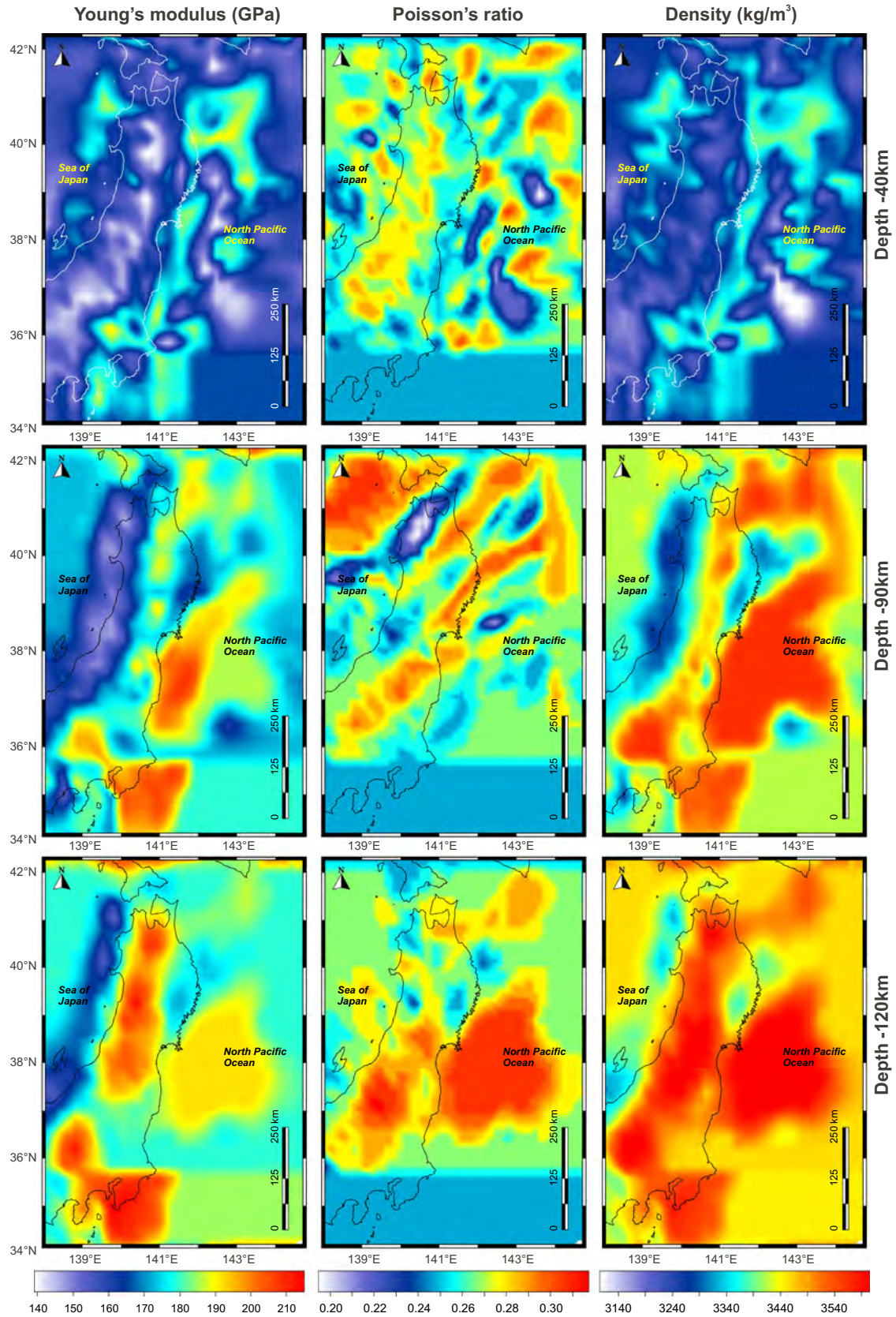
Young's modulus (GPa)   **Poisson's ratio**   **Density (kg/m³)**

Fig. 6. Young's modulus, Poisson's ratio and density for the heterogeneous model at three levels: −40, −90 and −120 km (b.s.l.).

orientation of the observed vectors. In proximity of FUKU station, strike-slip is instead slightly augmented and the vector turns anti-clockwise, in order to match the direction of the observed displace-

ment vector. Finally, for the vertical component, the amplitudes of the vectors at KAMN and KAMS are reduced, the amplitude of the vector at MYGI is augmented, and the vector at FUKU is now
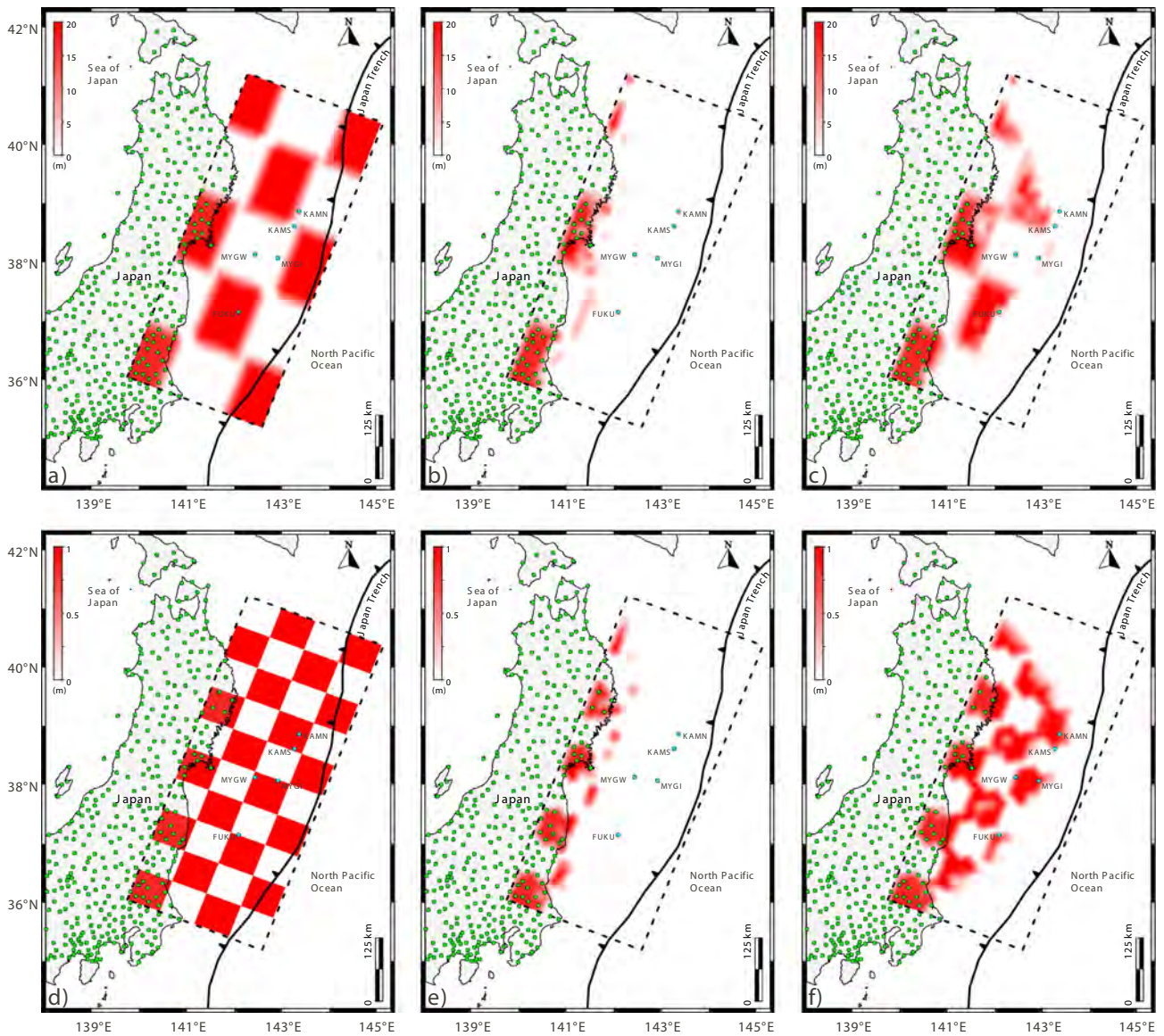
Fig. 7. Resolution tests. (a) and (d) Target models (5 × 3 patches – slip 0 or 20 m; 10 × 4 patches – slip 0 or 1 m) used for the checkerboard resolution tests. (b) and (e) Results of the checkerboard tests for inversion of the inland GPS data, exclusively. (c) and (f) Results of the checkerboard tests for inversion of both the inland and offshore data.

reduced even if it remains oriented downward, opposite to the recorded direction. Similarly, our optimization is not able to find a negative vertical displacement for MYGW station but the amplitude of the vector at this station is now strongly reduced.

Fig. 8 shows the comparison for the vertical component of displacement vectors at ground and offshore stations for three different optimized solutions: (1) stratified with flat surface (Fig. 8a), (2) stratified with DEM (Fig. 8b) and (3) heterogeneous with flat surface (Fig. 8c). Vectors for horizontal component are not shown because there are no evident changes for the above cases.

The comparison between Fig. 8a and b allows evaluating the contribution of the DEM in the optimization procedure. When a DEM is applied, vectors at two offshore stations are improved. In particular, the vectors at FUKU and KAMN stations show an improved fit with respect to the recorded data, while, at the remaining seafloor stations, the vertical displacement is increased and, therefore, worsened. It is noteworthy that, in particular, FUKU shows now a light positive vertical displacement as actually recorded. The standard deviation for the vertical component is increased from 0.130 to 0.140. Moreover, the standard deviation

for the horizontal components is also increased from 0.429 to 0.437 (Table 3). Fig. 8a and c show the contribution of the lateral heterogeneities (Fig. 8c), with respect to the stratified model (Fig. 8a). A positive contribution of the heterogeneities is found at MYGW and FUKU stations. For the former, the vector is reduced while the latter is increased. Vectors at other stations remain almost unchanged. In general, the use of the heterogeneities improves the value of the total standard deviation. We obtain a value of 0.434, smaller than the values obtained in the case stratified with (0.459) or without DEM (0.449), see Table 3. The positive contributions of the use of the DEM at KAMN station and, in particular, at FUKU station, showing now a light uplift as actually recorded, and, moreover, the obtained decrease of the total standard deviation using medium heterogeneities, prompted us to evaluate the case of a heterogeneous domain with DEM. Results for this case in Fig. 9. As expected, in this case, we have both the advantages of lateral heterogeneities as well as the surface relief at some stations (e.g., FUKU shows now a clear uplift as recorded). In particular, the combined model (medium heterogeneities with DEM) correctly images all recorded vertical
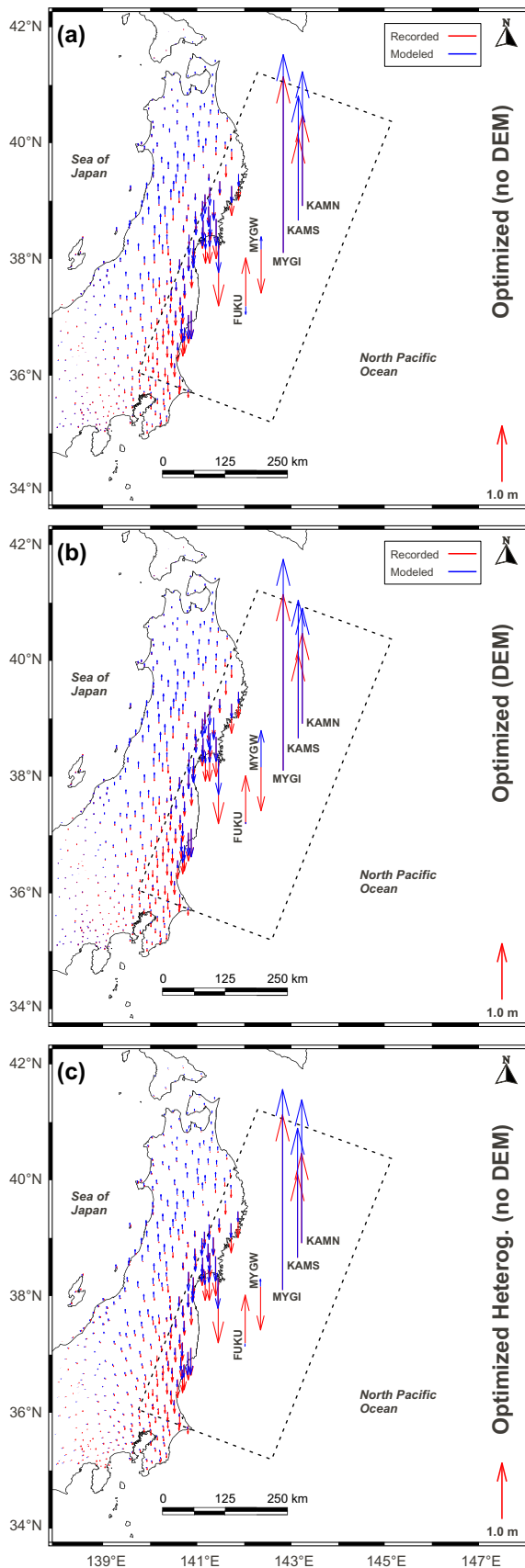
Fig. 8. Vertical component vectors for the cases: (a) optimized stratified model with flat surface; (b) optimized stratified model with DEM; (c) optimized heterogeneous model with flat surface.

displacements at the seafloor stations except at MYGW which is positive instead of negative. This last result however appears also in other inversions (e.g., Gusman et al., 2012; Romano et al., 2012).

As can be seen from Table 3 (which summarizes the total, horizontal and vertical standard deviations for all the cases previously described), the high values of the standard deviation of the direct model are greatly decreased by all the optimized solutions. Moreover the contribution of the DEM is to improve the vertical component at some stations (in particular, FUKU; see Fig. 9) while the lateral heterogeneities improve the horizontal components as expected (see Table 3).

The average rake angle from the slip distribution is 88° (Fig. 9) which is equal to the rake angle at the centroid (see Global CMT, http://www.globalcmt.org/) and to the rake found in Gusman et al. (2012). The slip pattern shows two areas with a maximum value of about 30 meters up-dip the hypocenter (orange star in Fig. 10b) and near the trench (light grey ellipse in Fig. 10b); these values are consistent with other results achieved independently by other researchers (Gusman et al., 2012; Koketsu et al., 2011).

Vertical displacements over the modelled fault plane, at free surface, are showed in Fig. 11. The maximum vertical displacement is around 4 m.

Two additional important results can be achieved from the complete heterogeneous model with DEM. From the results of a quadruple joint inversion of strong motions, teleseismic, geodetic and tsunami datasets, Yokota et al. (2011) infer the existence of a compact shallow rupture northeastwards of the hypocenter, which may be a usual fault slip (white ellipse in Fig. 10a). Here, we verify these results with the optimized displacement distribution for the most complete case (heterogeneous with DEM). The comparison in Fig. 10 shows that in our model no compact rupture is found to the east in that area. This result is consistent with the result of Koketsu et al. (2011) for separate strong motion, teleseismic and geodetic inversions. Yokota et al. (2011) also make the hypothesis that an area with inelastic properties should be present southwards of the compact rupture (blue ellipse in Fig. 10a). This hypothesis comes from the fact that, in their joined inversion, there is no slip eastwards of the epicenter (near the trench) as instead the separate inversion of tsunami data shows. In our model, this area of displacement near the trench is found independently of the use of tsunami data. The presence of a large slip distribution very near to the trench has been found also by Lay et al. (2011b).

Moreover, considering the opposite polarity of the up-down component of recorded displacements at MYGY and MYGW (Fig. 9), Sato et al. (2011) suppose that a polar reversal of the vertical displacements from downward to upward (as expected from the upper plate rebound) occurs at east of MYGW station. The hypothesis cannot however be verified directly by them because of the small number of stations, which represent a poor constraint. Is also noteworthy to underline that coastal areas that subside during the interseismic period (e.g., Suwa et al., 2006) also subsided during the Tohoku earthquake, therefore the earthquake did not simply reverse the accumulated interseismic motions. However, in order to verify the assumption about the boundary of polar reversal of the vertical displacements, we used the possibility of FEM to perform a blind prediction in a "near-real simulation", by looking at the horizontal and vertical displacements offshore, even in the areas where no stations are present. In particular, using the result of the optimization with heterogeneities and DEM, we built a map of these displacements (Fig. 11). The resulting map suggests that the beginning of the area of subsidence is not at east of MYGW. In our results, the area of polar reversal of the vertical displacements (PR) starts instead further at west of MYGW. At MYGW latitude, and considering the length scale of Fig. 11, the distance between our zero vertical displacement contour line (at west of

Table 3
Comparison of total, horizontal and vertical standard deviations of GPS and acoustic stations for all simulations.

| Simulation	Total standard deviation	Horizontal standard deviation	Vertical standard deviation
Direct model	1.113	1.086	0.245
Optimized no DEM	0.449	0.429	0.130
Optimized with DEM	0.459	0.437	0.140
Optimized Heterog. no DEM	0.434	0.414	0.131
Optimized Heterog. with DEM	0.444	0.422	0.137
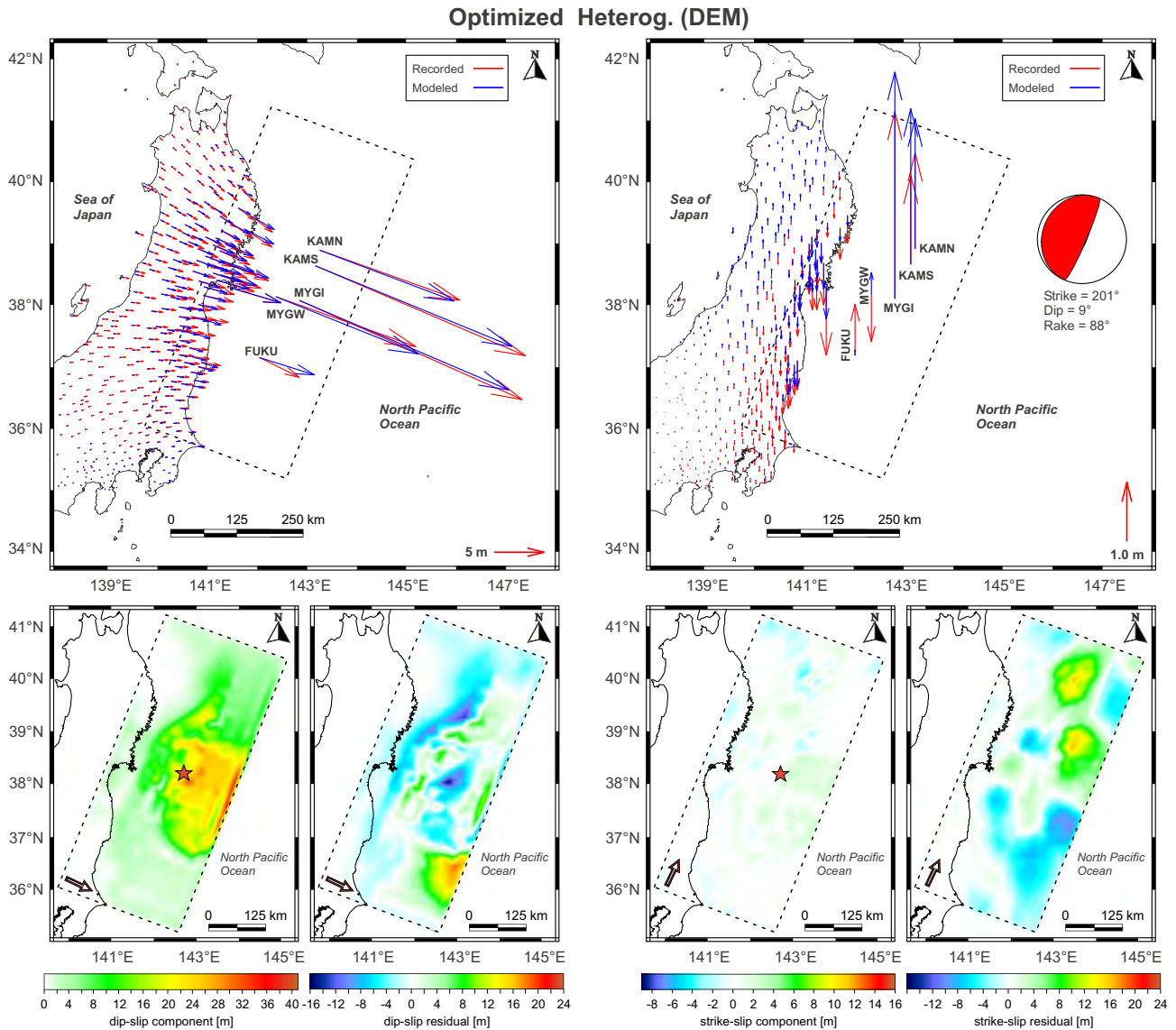
Fig. 9. Displacements for the optimized heterogeneous model with DEM. (Top left) Horizontal component vectors; (Top right) Vertical component vectors; (Bottom left) Fault slip distribution for the tangential component dip-slip (left) and difference respect to the "initial solution" (right); Bottom right) Fault slip distribution for the tangential component strike-slip (left) and difference respect to the "initial solution" (right). Red arrows in the bottom figures indicate the positive direction for the tangential components. Red star indicates the earthquake epicenter. The focal mechanism deduced by our optimization using the mean fault slip estimated in a range of about 50 km, around the hypocentral area is also reported. (For interpretation of the references to colour in this figure legend, the reader is referred to the web version of this article.)

MYGW) and the one supposed by Sato et al. (2011) at east of MYGW can be estimated to be about 50 km and then we believe that our result should be taken into consideration. If this is the case, the downward vertical displacement of MYGW should have another cause. The results of our model allowed us to identify the presence of two local anomalous areas (LA in Fig. 11) which can affect the estimation of the vertical component of displacement for the stations located nearby.

Finally, we tried to extend the blind prediction for the vertical displacement to the overall area of our model. In this condition, assuming the overall deformation path to be driven by the optimized solution for the GPS and acoustic stations and considering that the medium response at surface should reflect the used material properties included with the tomography (Young's modulus, Poisson's ratio and density) and the topographic reliefs, the plot of the contour lines of the zero vertical displacement in the north
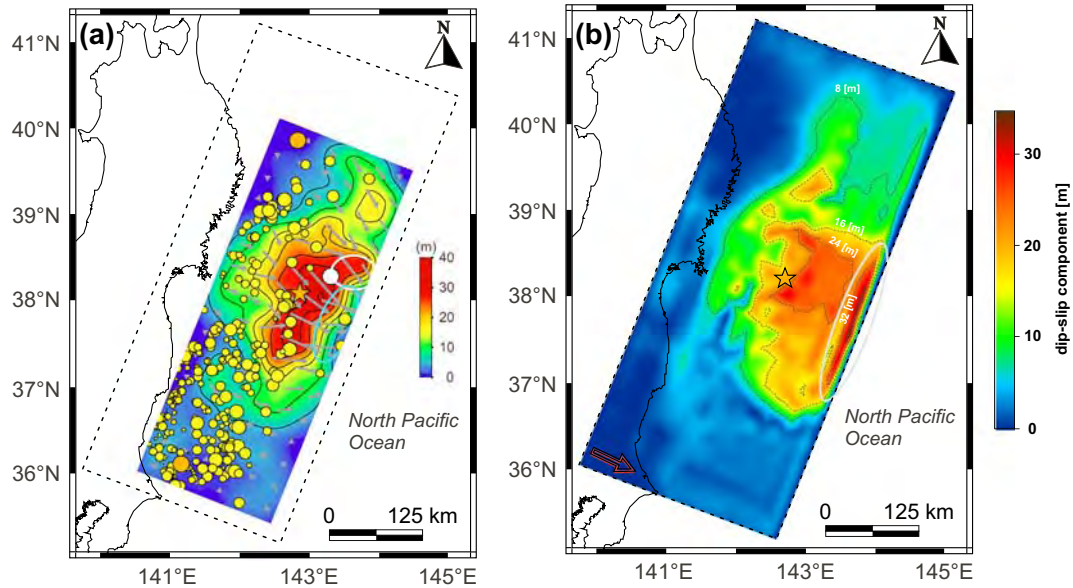
Fig. 10. Comparison between the total displacement as found from quadruple joint inversion (Yokota et al., 2011) and our FEM optimization (component dip-slip in this work). Part 9a modified from Yokota et al. (2011). Orange star indicates the earthquake epicenter. (For interpretation of the references to colour in this figure legend, the reader is referred to the web version of this article.)
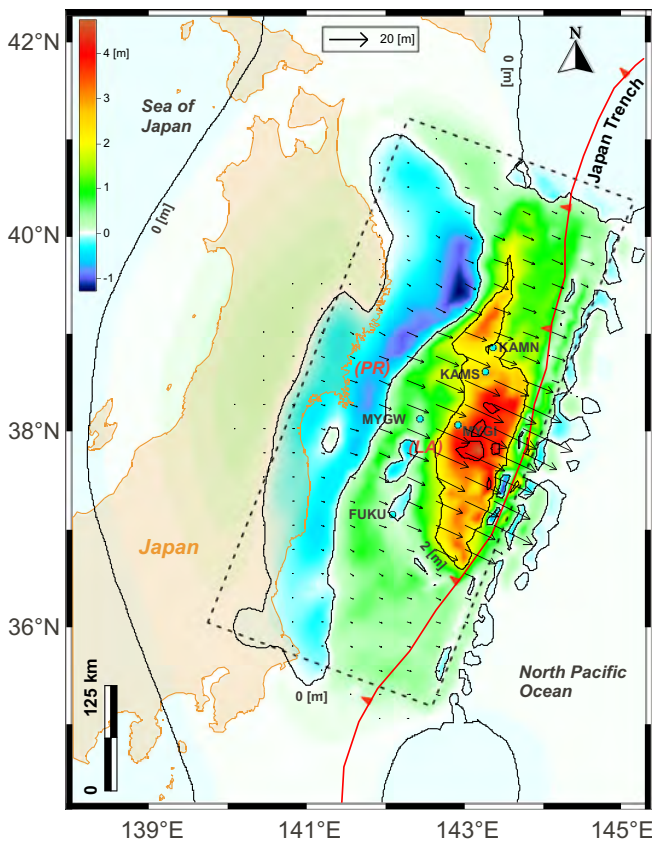
Fig. 11. Map of the overall deformation pattern for the optimized heterogeneous model with DEM. Vectors represent the horizontal component while colors and contour lines are for vertical component. The Figure shows that the polar reversal area for the vertical displacements (PR) starts further west of MYGW station. See text for details.

Japan area suggest the presence of three distinct sectors: (1) an inversion of the vertical displacement close to the Japan trench westward (from negative to positive), (2) the area of the polar reversal of the vertical displacements previously discussed which is in correspondence of the North East Japan Arc, and, (3) another inversion in the area (from positive to negative) at the boundary between the Ohkotsk and the Amurian Plate where the latter subducts under the former. The shape and location of this last limit has been separately confirmed by previous researchers basing on GPS data (Heki et al., 1999; Jin et al., 2007). We then speculate that the contour lines with zero vertical displacements are implicitly describing the response of the medium in zones of transition where the elastic properties change. All these important results described above, give a valuable clue on the kinematic of Japan, in terms of the response of the crust to the subduction process and may find further confirmation, upon the installation of new stations inland and offshore.

5. Discussions and conclusions

An optimized 3D finite element model to study the relationship between the slip distribution at the fault plane and the coseismic displacements at the surface, during the 11 March 2011 Tohoku Oki earthquake, has been performed. The model is highly realistic including the position and rheologies of the Pacific and Okhotsk plates, a digital elevation model of the free surface (DEM) and the fault plane, as inferred from CJAGC. The solution of the finite fault inversion provided by CJAGC, here called "initial solution", fits well the coseismic displacements at GPS stations in the FEM environment, but is not able to fit the displacements at five acoustic transponders located on the ocean floor, around the earthquake epicenter (Fig. 5). At offshore stations, modelled vectors show big differences in terms of amplitude and direction (both for the horizontal and vertical components) with respect to the observed ones. Starting from the "initial solution", an optimization procedure was developed with the aim of re-computing the slip distribution on the fault plane including the offshore data. To take different possible cases into account, we considered two different rheological settings: (1) a stratified layered velocity model with an isotropic PREM (which is the same configuration used to infer the "initial solution") and (2) a highly realistic heterogeneous model which takes account of precise v_p and v_s velocities (Zhao, 2009). Both

these configurations are tested considering or a flat surface or a DEM (topography data from Smith and Sandwell, (1997)). When the "initial solution" is used in a direct model, the vectors of the GPS stations computed numerically show a general good fit with respect to the observed displacement vectors (Fig. 3). This means that the absence of lateral variations in the "initial solution" is not important to describe correctly the deformation path. However, this is true if only ground GPS stations are considered. Indeed, (see Table 3), when GPS and acoustic stations are considered both, the application of lateral and vertical heterogeneities (Optimized Heterogeneous no DEM) with respect to the vertical heterogeneities only (Optimized no DEM) becomes important, since it improves the Total Standard Deviation and in particular the Horizontal Standard Deviation.

In a first simulation, the original fault slip distribution ("initial solution") has been optimized in the same physical and geometrical conditions used to acquire it (flat surface and stratified vertical heterogeneous domain). In this case, the optimized solution already greatly improves all the misfits that the "initial solution" had offshore by creating a new slip distribution onto the fault plane which tends to enforce the N110°E tangential component (dip-slip), in the most eastern part, to decrease it in the southeastern part and to strongly reduce the N20°E tangential component (strike-slip) almost everywhere. The new fault slip distribution still keeps a good agreement with the ground GPS stations (Fig. 5).

Successively, the DEM was considered. The DEM does not affect the horizontal component but it is important for the vertical component at some stations like FUKU and KAMN (Fig. 8). At the position of GPS stations, the DEM does not change the vectors since the topography in Japan does not have big height variations. On the contrary, for the offshore stations, which are located at some kilometers below sea level, the use of the bathymetry is essential. It is found that the vertical vectors at FUKU and KAMN stations show an improved fit with the recorded data. In particular, FUKU shows now a light positive vertical displacement as actually recorded (Fig. 8b). Contrarily, in the optimization without DEM, FUKU station showed a downlift (Fig. 8a).

Successively, we considered the contribution of medium heterogeneities with respect to the stratified model. In this case, no DEM is considered to avoid possible disturbances coming from the use of the topography. The inclusion of the lateral heterogeneities generally improves the horizontal component (as can be seen from the standard deviation with respect to the stratified case – Table 3) and fixes the vertical displacement offshore for MYGW and FUKU stations (compare Fig. 8a and c).

Therefore, a complete model including both the medium heterogeneities and the DEM was considered (Fig. 9). This model shows a good fit between modelled and observed displacements at GPS and offshore stations and improves further the overall displacement path by decreasing the total standard deviation with respect to the stratified layered velocity case (Table 3).

Moreover, from the complete model two other important results are extracted (Fig. 10). The first is the absence of a shallow compact region northeastwards of the fault plane, considered in Yokota et al. (2011) but excluded in Koketsu et al. (2011). In Yokota et al. (2011) an area with inelastic deformation southwards of the compact rupture is also considered (blue ellipse in Fig. 10a) to improve the fit of the observed and synthetic tsunami waveforms to the level of the separate tsunami inversion. In our result, instead, this area appears without considering tsunami dataset (light grey ellipse in Fig. 10b). Moreover, our result (Fig. 10b) is similar to the slip distribution inverted by Ozawa et al. (2012), that used also seafloor displacements (see their Fig. 7c). In particular, the estimated coseismic slip distribution obtained in this study and by Ozawa et al. (2012) is more consistent with the location of the 2011 Tohoku earthquake, respect to the result obtained

not taking seafloor deformation into account (Ozawa et al., 2011). Another important result derives from the map of the overall displacement pattern at the free surface (Fig. 11). The map shows that MYGW station is not located at west of the frontier of the polar reversal zone (separation between the positive and the negative vertical displacement; PR in Fig. 11), as hypothesized by Sato et al. (2011). Indeed, we found the presence of two local anomalies (LA) which may affect the determination of the displacement at MYGW and FUKU. Moreover, we found that the hinge line, demarcating the beginning of the polar reversal of the vertical displacements, expected from the upper plate rebound, is instead on the other side of MYGW, at west, and almost coincident with the Northern Japan Arc position (PR in Fig. 11).

Finally, by performing an overall blind prediction, we checked for the total (all the top surface of our domain) vertical deformation pattern and plotted the zero vertical displacement contours lines. In this case another line appears at west, very close to the eastern limit of the Amurian Plate, whose shape and location has been similarly inferred by other researches basing on GPS data (Heki et al., 1999; Jin et al., 2007). We speculate that the presence of different material properties at the border between the two plates (which are included in our model) can explain the observed zero vertical displacement contour line.

In conclusion, the results previously described give new insights in terms of the earthquake dynamics, providing a new image of the fault slip distribution with important suggestions on the areas most involved by the subduction process. Moreover, a better view of the kinematic of the north Japan area has been provided.

Appendix A. Supplementary data

Supplementary data associated with this article can be found, in the online version, at http://dx.doi.org/10.1016/j.pepi.2014.09.003.

References

Aloisi, M., Cocina, O., Neri, G., Orecchio, B., e Privitera, E., 2002. Seismic tomography of the crust underneath the Etna volcano, Sicily. Phys. Earth Planetary Interiors 134, 139–155. http://dx.doi.org/10.1016/S0031-9201(02)00153-X.

Aloisi M., Mattia M., Monaco C. e Pulvirenti F., 2011. Magma, faults, and gravitational loading at Mount Etna: The 2002–2003 eruptive period. J. Geophys. Res. – Solid Earth, 116, B05203, http://dx.doi.org/10.1029/2010JB007909.

Amici S., Anzidei M., Bignami C., Brunori C.A., Borgstrom S., Buongiorno F., Cheloni D., Chini M., Cinti F. R., D'Agostino N., De Martini P.M., Fornaciai A., Gambino S., Guglielmino F., Kyriakopoulos C., Lorito S., Melini D., Merucci L.,

Moro M., Nappi R., Pantosti D., Piatanesi A., Piscini A., Puglisi G., Riguzzi F., Romano F., Silvestri M., Siniscalchi V., S. Stramondo., 2013. The March 11th, 2011, M 9.0 earthquake offshore Honshu island (Japan): a synthesis of the Tohoku-Oki INGV Team research activities. Quaderni di Geofisica, Number 105, ISSN 1590–2595.

Ammon, C.J., Lay, T., Kanamori, H., Cleveland, M., 2011. A rupture model of the great 2011 Tohoku earthquake. Earth Planets Space 63, 693–696. http://dx.doi.org/10.5047/eps.2011.05.015.

Bassin, C., Laske, G., Masters, G., 2000. The current limits of resolution for surface wave tomography in North America. EOS Trans AGU 81, F897.

Cattin, R., Briole, P., Lyon-Caen, H., Bernard, P., Pinettes, P., 1999. Effects of superficial layers on coseismic displacements for a dip-slip fault and geophysical implications. Geophys. J. Int. 137, 149–158. http://dx.doi.org/10.1046/j.1365-246X.1999.00779.x.

Chu, R., Wei, S., Helmberger, V., Zhan, D., Zhu, Z., Kanamori, L.H., 2011. Initiation of the great M w 9.0 Tohoku-Oki earthquake. Earth Planetary Science Lett. 308, 277–283. http://dx.doi.org/10.1016/j.epsl.2011.06.031.

Christensen, N.I., Mooney, W.D., 1995. Seismic velocity structure and composition of the continental crust: a global view. J. Geophys. Res. 100, 9761–9788. http://dx.doi.org/10.1029/95JB00259.

Davis, C., Keilis-Borok, V., Kossobokov, V., Soloviev, A., 2012. Advance prediction of the March 11, 2011 Great East Japan Earthquake: a missed opportunity for disaster preparedness. Int. J. Disaster Risk Reduction 1, 17–32. http://dx.doi.org/10.1016/j.ijdrr.2012.03.001.

DeMets, C., Gordon, R.G., Argus, D.F., Stein, S., 1990. Current plate motions. Geophys. J. Int. 101 (2), 425–478. http://dx.doi.org/10.1111/j.1365-246X.1990.tb06579.x.

Dziewonski, A.M., Anderson, D.L., 1981. Preliminary reference Earth model. Phys. Earth Planetary Interiors 25, 297–356.

Eberhart-Phillips, D., 1986. Three-dimensional velocity structure in Northern California Coast Ranges from inversion of local earthquake arrival times. Bull. Seismol. Soc. Am. 76, 1025–1052.

Fujii, Y., Satake, K., Sakai, S., Shinohara, M., Kanazawa, T., 2011. Tsunami source of the 2011 off the Pacific coast of Tohoku Japan earthquake. Earth Planets Space 63, 815–820. http://dx.doi.org/10.5047/eps.2011.06.010.

Fujita M., Ishikawa T., Mochizuki M., Sato M., Toyama S., Katayama M., Kawai K., Matsumoto Y., Yabuki T., Asada A., Colombo O. L., 2006. GPS/Acoustic seafloor geodetic observation: method of data analysis and its application, Earth Planets Space, 58, 265–275, ISSN: 1343–8832.

Gill P., Murray W., Saunders A., 2006. User's Guide for SNOPT Version 7: Software for Large-Scale Nonlinear Programming. Stanford University - Business Software Inc.

Grilli, S.T., Harris, J.C., Tajalli Bakhsh, T.S., Masterlark, T.L., Kyriakopoulos, C., Kirby, J.T., Shi, F., 2012. Numerical simulation of the 2011 Tohoku Tsunami based on a new transient fem co-seismic source: comparison to far- and near-field observations. Geophys, Pure Appl. http://dx.doi.org/10.1007/s00024-012-0528-y.

Gusman, A.R., Tanioka, Y., Sakai, S., Tsushima, H., 2012. Source model of the great 2011 Tohoku earthquake estimated from tsunami waveforms and crustal deformation data. Earth Planetary Science Lett. 341–344, 234–242. http://dx.doi.org/10.1016/j.epsl.2012.06.006.

Hasegawa, A., Nakajima, J., Umino, N., Miura, S., 2005. Deep structure of the northeastern Japan arc and its implications for crustal deformation and shallow seismic activity. Tectonophysics 403, 59–75. http://dx.doi.org/10.1016/j.tecto.2005.03.018.

Heki, K., Miyazaki, S., Takahashi, H., Kasahara, M., Kimata, F., Miura, S., Vasilenko, N.F., Ivashchenko, A., An, K., 1999. The Amurian plate motion and current plate kinematics in eastern Asia. J. Geophys. Res. 104. http://dx.doi.org/10.1029/1999JB900295.

Hirose, H., 2011. Tilt records prior to the 2011 off the Pacific Coast of Tohoku Earthquake. Earth Planets Space 63 (1–7), 655–658. http://dx.doi.org/10.5047/eps.2011.05.009.

Hsu Y.J., Simons M., Williams C., Casarotti E., 2011. Three-dimensional FEM derived elastic Green's functions for the coseismic deformation of the 2005 M_w 8.7 Nias-Simeulue, Sumatra earthquake. Geochem. Geophys. Geosyst. volume 12, Number 7, http://dx.doi.org/10.1029/2011GC003553.

Iinuma T., Hino R., Kido M., Inazu D., Osada Y., Ito Y., Ohzono M., Tsushima H., Suzuki S., Fujimoto H., S. Miura. 2012. Coseismic slip distribution of the 2011 off the Pacific Coast of Tohoku Earthquake (M9.0) refined by means of seafloor geodetic data, J. Geophys. Res. 117, B07409, http://dx.doi.org/10.1029/2012JB009186.

Ide, S., Baltay, A., Beroza, G., 2011. Shallow dynamic overshoot and energetic deep rupture in the 2011 M w 9.0 Tohoku-Oki earthquake. Science 332, 1426–1429. http://dx.doi.org/10.1126/science.1207020.

Ji, C., Wald, D.J., Helmberger, D.V., 2002. Source description of the 1999 Hector Mine, California earthquake; Part I: Wavelet domain inversion theory and resolution analysis. Bull. Seism. Soc. Am. 92 (4), 1192–1207. http://dx.doi.org/10.1785/0120000917.

Jin, S., Park, P., Zhu, W., 2007. Micro-plate tectonics and kinematics in Northeast Asia inferred from a dense set of GPS observations. Earth Planet Sci. Lett. 257, 486–496. http://dx.doi.org/10.1016/j.epsl.2007.03.011.

Kobayashi, T., Tobita, M., Nishimura, T., Suzuki, A., Noguchi, Y., Yamanaka, M., 2011. Crustal deformation map for the 2011 off the Pacific coast of Tohoku Earthquake, detected by InSAR analysis combined with GEONET data. Earth Planets Space 63, 621–625. http://dx.doi.org/10.5047/eps.2011.06.043.

Koketsu, K., Yokota, Y., Nishimura, N., Yagi, Y., Miyazaki, S., Satake, K., Fujii, Y., Miyake, H., Sakai, S., Yamanaka, Y., Okada, T., 2011. A unified source model for the 2011 Tohoku earthquake, Earth Planet. Sci. Lett. 310, 480–487. http://dx.doi.org/10.1016/j.epsl.2011.09.009.

Kyriakopoulos, C., Masterlark, T., Stramondo, S., Chini, M., Bignami, C., 2013. Coseismic slip distribution for the M_w 9 2011 Tohoku-Oki earthquake derived from 3-D FE modeling. J. Geophys. Res. Solid Earth 118, 10.1002/jgrb.50265.

Lay T., Ammon C. J., Kanamori H., Kim M. J. and L. Xue, (2011a). Outer trench-slope faulting and the great 2011 Tohoku (Mw 9.0) earthquake, Earth Planets Space, http://dx.doi.org/10.5047/eps.2011.05.006.

Lay, T., Ammon, C.J., Kanamori, H., Xue, L., Kim, M.J., 2011b. Possible large near-trench slip during the 2011 M w 9.0 off the Pacific coast of Tohoku earthquake. Earth Planets Space 63, 687–692. http://dx.doi.org/10.5047/eps.2011.05.033.

Lee, S.J., 2012. Rupture process of the 2011 Tohoku-Oki Earthquake based upon joint source inversion of teleseismic and GPS data. Terr. Atmos. Ocean. Sci. 23 (1), 1–7. http://dx.doi.org/10.3319/TAO.2011.07.11.01(T).

Liu W. and F. Yamazaki, 2011. Estimation of crustal movements due to the 2011 Tohoku, Japan Earthquake from TerraSAR-X intensity images. Ninth International workshop on Remote Sensing for Disaster Response. Stanford University, September 15–16.

Masterlark, T., 2003. Finite element model predictions of static deformation from dislocation sources in a subduction zone: sensitivities to homogeneous, isotropic, Poisson-solid, and half-space assumptions. J. Geophys. Res. 108 (B11), 2540. http://dx.doi.org/10.1029/2002JB002296.

Minoura, K., Imamura, F., Sugawara, D., Kono, Y., Iwashita, T., 2001. The 869 Jogan tsunami deposit and recurrence interval of large-scale tsunami on the Pacific coast of northeast Japan. J. Nat. Disaster Sci. 23 (2), 83–88.

Nakajima, J., Hasegawa, A., 2006. Anomalous low-velocity zone and linear alignment of seismicity along it in the subducted Pacific slab beneath Kanto, Japan: reactivation of subducted fracture zone? Geophys. Res. Lett. 33, L16309. http://dx.doi.org/10.1029/2006GL026773.

Okada, Y., 1985. Surface deformation due to shear and tensile faults in half-space. Bull. Seismol. Soc. Am. 75, 1135–1154.

Ozawa, S., Nishimura, T., Suito, H., Kobayashi, T., Tobita, M., Imakiire, T., 2011. Coseismic and postseismic slip of the 2011 magnitude-9 Tohoku- Oki earthquake. Nature 475, 373–376. http://dx.doi.org/10.1038/nature10227.

Ozawa, S., Nishimura, T., Munekane, H., Suito, H., Kobayashi, T., Tobita, M., Imakiire, T., 2012. Preceding, coseismic, and postseismic slips of the 2011 Tohoku earthquake, Japan. J. Geophys. Res. B07404. http://dx.doi.org/10.1029/2011JB009120.

Pergler, T., Matyska, C., 2007. A hybrid spectral and finite element method for coseismic and postseismic deformation. Phys. Earth Planet. Inter. 163, 122–148. http://dx.doi.org/10.1016/j.pepi.2007.05.012.

Romano, F., Piatanesi, A., Lorito, S., D'Agostino, N., Hirata, K., Atzori, S., Yamazaki, Y., Cocco, M., 2012. Clues from joint inversion of tsunami and geodetic data of the 2011 Tohoku-oki earthquake. Scientific Reports 2, 385. http://dx.doi.org/10.1038/srep00385.

Sato, M., Ishikawa, T., Ujihara, N., Yoshida, S., Fujita, M., Mochizuki, M., Asada, A., 2011. Displacement above the hypocenter of the 2011 Tohoku-Oki earthquake. Science 332, 1395. http://dx.doi.org/10.1126/science.1207401.

Simons, M., Minson, S.E., Sladen, A., Ortegal, F., Jiang, J., Owen, S.E., Meng, L., Ampuero, J.P., Wei, S., Chu, R., Helmberger, D.V., Kanamori, H., Hetland, E., Moore, A.W., Webb, F.H., 2011. The 2011 magnitude 9.0 Tohoku-Oki earthquake: mosaicking the megathrust from seconds to centuries. Science 332, 1421–1425. http://dx.doi.org/10.1126/science.1206731.

Smith, W.H.F., Sandwell, D.T., 1997. Global seafloor topography from satellite altimetry and ship depth soundings. Science 277 (5334), 1957–1962. http://dx.doi.org/10.1126/science.277.5334.1956.

Suito, H., Izuka, M., Hirahara, K., 2002. 3-D Viscoelastic FEM modeling of crustal deformation in Northeast Japan. Pure appl. geophys. 159, 2239–2259. http://dx.doi.org/10.1007/978-3-0348-8197-5_5.

Suwa, Y., Miura, S., Hasegawa, A., Sato, T., Tachibana, K., 2006. Interplate coupling beneath NE Japan inferred from three-dimensional displacement field. J. Geophys. Res. 111 (B04402), 2004J. http://dx.doi.org/10.1029/B003203.

Taira, A., 2001. Tectonic evolution of the Japanese island arc system. Annu. Rev. Earth Planet Sci. 29, 109–134.

Trubienko O., Fleitout L., Garaud J.D., C. Vigny 2013. Interpretation of interseismic deformations and the seismic cycle associated with large subduction earthquakes, Tectonophysics, volume 589, 126-141, http://dx.doi.org/10.1016/j.tecto.2012.12.027.

Wang R., Parolai S., Ge M., Jin M., Walter T. R., Zschau J., 2013. The 2011 M_w 9.0 Tohoku Earthquake: comparison of GPS and strong-motion data. Bulletin of the Seismological Society of America, vol. 103, No. 2b, http://dx.doi.org/10.1785/0120110264.

Wei D., T. Seno, 1998. Determination of the Amurian plate motion, in Mantle dynamics and plate interactions in East Asia, Geodynamics. Series, 27, ed. by M. F. J. Flower, S. L. Chung, C. H. Lo, and T. Y. Lee, pp. 337–346, AGU, Washington D. C., http://dx.doi.org/10.1029/GD027p0337.

Yoshida, Y., Ueno, H., Muto, D., Aoki, S., 2011. Source process of the 2011 off the Pacific Coast of Tohoku earthquake with the combination of teleseismic and strong motion data. Earth Planets Space 58, 1–5. http://dx.doi.org/10.5047/eps.2011.05.011.

Yokota Y., Koketsu K., Fujii Y., Satake K., Sakai S., Shinohara M., Kanazawa T. 2011. Joint inversion of strong motion, teleseismic, geodetic, and tsunami datasets for the rupture process of the 2011 Tohoku earthquake. Geophys. Res. Lett. vol. 38, L00G21, http://dx.doi.org/10.1029/2011GL050098.

Zahradnik J., Gallovic F., Sokos E., G.A. Tselentis, 2011. Preliminary slip model of M9 Tohoku earthquake from strong-motion stations in Japan - an extreme application of ISOLA code. Report to EMSC.

Zhang, H., Ge, Z., Ding, L., 2011. Three sub-events composing the 2011 off the Pacific Coast of Tohoku Earthquake (M w 9.0) Inferred from rupture imaging by back projecting Teleseismic p waves. Earth Planets Space 63, 595–598. http://dx.doi.org/10.5047/eps.2011.06.021.

Zhao, D., Horiuchi, S., Hasegawa, A., 1992. Seismic velocity structure of the crust beneath the Japan Islands. Tectonophysics 212, 289–301. http://dx.doi.org/10.1016/0040-1951(92)90296-I.

Zhao, D., Hasegawa, A., Kanamori, H., 1994. Deep structure of Japan subduction zone as derived from local, regional and teleseismic events. J. Geophys. Res. 99, 22313–22329. http://dx.doi.org/10.1029/94JB01149.

Zhao, D., Matsuzawa, T., Hasegawa, A., 1997. Morphology of the subducting slab boundary in the northeastern Japan arc. Phys. Earth Planet. Inter. 102, 89–104. http://dx.doi.org/10.1016/S0031-9201(96)03258-X.

Zhao, D., 2009. Multiscale seismic tomography and mantle dynamics. Gondwana Res. 15, 297–323. http://dx.doi.org/10.1016/j.gr.2008.07.003.

Zhao, D., Huang, Z., Umino, N., Hasegawa, A., Yoshida, T., 2011. Seismic imaging of the Amur-Okhotsk plate boundary zone in the Japan Sea. Phys. Earth Planetary Interiors 188, 82–95. http://dx.doi.org/10.1016/j.pepi.2011.06.013.